Chemical Science

Accepted Manuscript

This article can be cited before page numbers have been issued, to do this please use: X. Lou, W. Liu, M. Yang, H. Zhang, J. Fan and X. Peng, *Chem. Sci.*, 2026, DOI: 10.1039/D6SC02492K.

ARTICLE Journal Name

# Invoking Ferroptosis and Photon-Controlled Pyroptosis via an Integrated Therapeutic System for Triple-Pathway Tumor Therapy

View Article Online
DOI: 10.1039/D6SC02492K

Received 00th January 20xx,
Accepted 00th January 20xx

DOI: 10.1039/x0xx00000x

Xue Lou, †[a] Wenkai Liu, †[c] Mingwang Yang, [a] Hua Zhang, *[b] Jiangli Fan, *[a] Xiaojun Peng [a]

Antitumor agents that rely solely on apoptosis often fail to disrupt the complementary cell survival cascades. In this study, we developed a redox-responsive integrated therapeutic system (QSH) that exploited ferroptosis and pyroptosis to enhance tumor therapy. QSH consisted of a dihydroorotate dehydrogenase (DHODH in mitochondria) inhibitor (Q, a ferroptosis inducer) and a photosensitiser (IHcy, a pyroptosis trigger) linked by a disulphide bond. Upon entering cancer cells, QSH could effectively target mitochondria by leveraging the mitochondrial membrane potential. Within the highly redox-stressed tumor microenvironment, the disulfide bonds were cleaved by glutathione (GSH), leading to the release of Q and IHcy, which promoted glutathione peroxidase 4 (GPX4)-mediated ferroptosis (the first pathway). The released Q inhibited DHODH activity within mitochondria, thereby disrupting the DHODH-mediated mitochondrial antioxidant system and also promoting ferroptosis (the second pathway). Under light irradiation, the photodynamic effect of IHcy triggered gasdermin D (GSDMD)-mediated pyroptosis (the third pathway), thereby promoting the release of damage-associated molecular patterns. Significantly, QSH completely suppressed tumor growth in 4T1 breast cancer models due to the synchronous activation of ferroptosis and pyroptosis in tumors. This redox-triggered triple-pathway strategy effectively elevated the level of lipid peroxidation within cells, induced immunogenic cell death, and enhanced tumor sensitivity to treatments.





## Introduction

Cell death plays a fundamental role in maintaining homeostasis and facilitating the development of multicellular organisms.[1] It is broadly classified into two categories: programmed cell death (PCD) and accidental cell death (ACD).[2] ACD is typically triggered by severe physical, chemical, or mechanical insults, whereas PCD is an active, tightly regulated process encompassing multiple distinct mechanisms, including apoptosis, ferroptosis, and pyroptosis.[3] Due to its controllability, PCD has emerged as a cornerstone of cancer therapy.[4] Although ferroptosis exploits the inherent metabolic vulnerabilities to tumour cells and pyroptosis provokes robust immunogenic responses, current mainstream treatments-such as chemotherapy and radiotherapy-primarily focus on activating the classical apoptotic pathway.[5-11] However, due to the complexity of the tumour microenvironment and the inherent heterogeneity of cancer cells, relying solely on apoptosis often leads to suboptimal therapeutic outcomes.[12-14] This underscores the urgent need to explore non-apoptotic forms of cell death to eliminate apoptosis-insensitive tumour cells.

Pyroptosis, a highly inflammatory form of PCD, is characterised by membrane pore formation, cellular swelling, and eventual membrane rupture.[15,16] Inducing pyroptosis in tumor cells not only eliminates these malignant cells but also triggers the release of damage-associated molecular patterns (DAMPs). This process further promotes the immunogenic cell death (ICD) of tumour cells, thereby enhancing the their sensitivity to subsequent therapeutic interventions.[17] Pyroptosis can be induced by diverse stimuli such as pathogen components (flagellin), danger signals (adenosine triphosphate, ATP), or chemotherapeutic drugs (cisplatin).[18-20] Furthermore, photodynamic therapy (PDT) is an emerging, non-invasive therapeutic strategy that employs photosensitizers to generate reactive oxygen species (ROS) upon light exposure, thereby inducing cancer cells death.[21-25] Notably, during PDT, certain photosensitizers can regulate cancer cells death by inducing pyroptosis, that is photon-controlled pyroptosis activation (PhotoPyro).[26-29] As a novel strategy that combines spatially controllable phototherapy with pyroptosis-mediated ICD, PhotoPyro offers promising potential in enhancing the host's antitumor immunity, overcoming therapeutic resistance in tumour cells, and improving treatment specificity.[30-33] However, in the tumour microenvironment, the efficacy of PhotoPyro is compromised by inherent antioxidant defence systems (e.g., Glutathione, Superoxide Dismutase, Catalase) that scavenge ROS and attenuate their cytotoxic effect, leading to restricted therapeutic effects.[34]

Ferroptosis is a form of iron-dependent cell death characterised by the accumulation of uncontrolled lipid peroxidation (LPO).[35,36] It is counteracted by intricate intracellular antioxidant systems,[37] primarily the glutathione peroxidase 4 (GPX4) pathway and the dihydroorotate dehydrogenase (DHODH) system, which help tumour cells evade ferroptotic death.[38-40] GPX4 is a key regulator that inhibits LPO by neutralising lipid peroxides.[41,42] In parallel, the DHODH pathway represents an independent mitochondrial defence mechanism.[43, 44] Therefore, the simultaneous inhibition of GPX4 and DHODH can promote ferroptosis, and the LPO generated

[a] State Key Laboratory of Fine Chemicals, Frontiers Science Center for Smart Materials, Dalian University of Technology, Dalian 116024, P. R. China.
[b] School of Chemistry and Chemical Engineering, Henan International Joint Laboratory of Smart Molecules and Identification and Diagnostic Functions, Henan Normal University, Henan 453007, P. R. China.
[c] College of Chemical Engineering and Environment, Weifang University of Science and Technology, Weifang 262700, P. R. China.
† X. Lou and W.K. Liu contributed equally to this work.

View Article Online
DOI: 10.1039/D6SC02492K



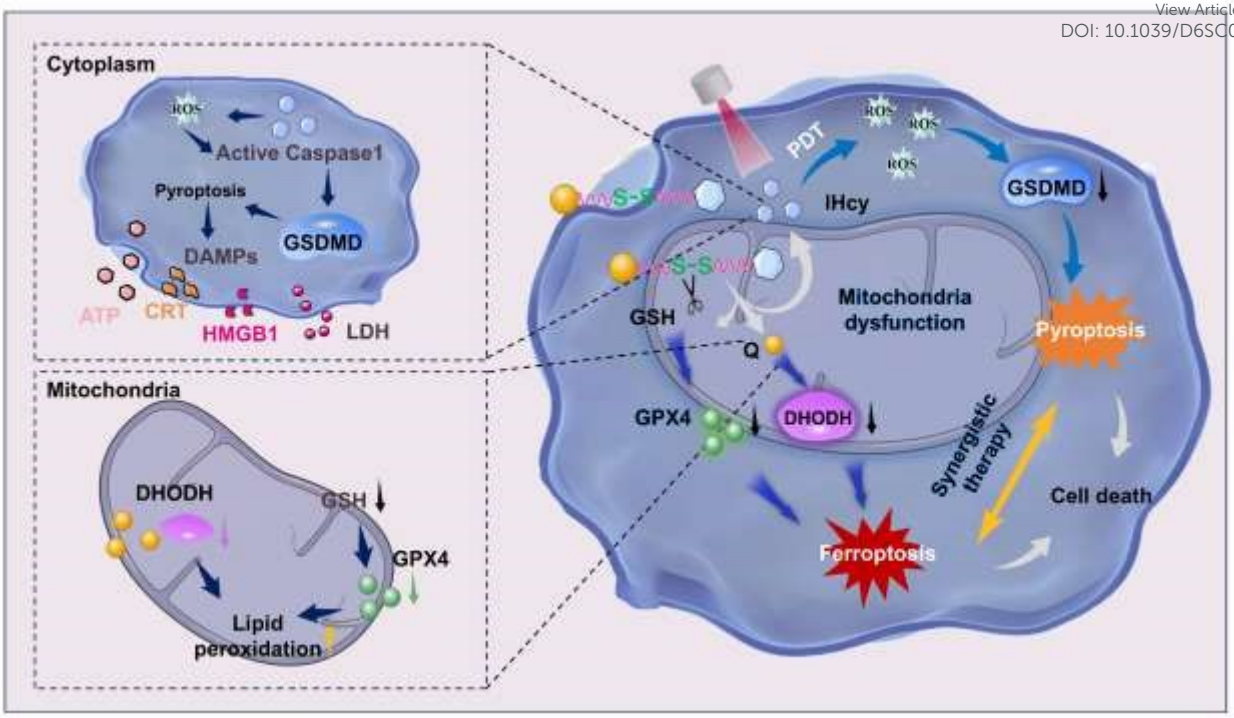


**Scheme 1.** Schematic illustration of the antineoplastic mechanism of QSH. The cleavage of the disulfide bond and the inhibition of DHODH by the released Q induce ferroptosis, while IHcy promotes the generation of ROS, triggering pyroptosis and thereby facilitating synergistic therapeutic effects.

during ferroptosis contributes to ROS accumulation, which in turn enhances the efficacy of PhotoPyro. Additionally, pyroptosis initiated by ROS accumulation can reshape the tumour microenvironment, and further increase tumour susceptibility to ferroptosis.[45] Therefore, PhotoPyro and ferroptosis can benefit from each other by integrating their respective advantages to achieve win-win cooperation. Unfortunately, current strategies typically employ the co-administration of separate ferroptosis- and pyroptosis-inducing agents or cocktail nanoplatforms, these approaches often suffer from inconsistent drug distribution, complex pharmacokinetics, and potential off-target effects.[46]

In this study, we strategically designed a distinctive unimolecular phototherapeutic agent (QSH) capable of activating three pathways to achieve synergistic tumour therapy through coordinated ferroptosis and pyroptosis. QSH was constructed by connecting a photosensitizer (IHcy) with a DHODH inhibitor (Q) via a thiol disulphide bond. Once trapped in cancer cells, QSH would efficiently target mitochondria through mitochondrial membrane potential driven accumulation of the cation. In the highly redox-stressed tumour microenvironment, the thiol disulphide bond of QSH were cleaved by GSH,[35] leading to the release of Q and IHcy. This represented the first pathway for ferroptosis activation, as the depletion of GSH (a critical cofactor of GPX4), compromised GPX4 activity and cellular antioxidant defence. The released Q also enhanced LPO through inhibition of DHODH activity, thereby further promoting ferroptosis, representing the second pathway. Upon near-infrared (NIR) light (690 nm) irradiation, ROS generated by the released IHcy activated the third pathway, GSDMD-mediated pyroptosis, and facilitated the release of pyroptosis-associated DAMPs. These characteristics were validated through multiple lines of evidence, including impaired mitochondrial function and altered morphology, as well as downregulation of associated protein expression. Collectively, these findings suggested that QSH not only induced ferroptosis mediated by dual pathways, but also triggered pyroptosis that could promote immunogenic cell death (ICD) of tumours (Scheme 1). This unimolecular-based, triple-pathway strategy represents a promising approach to overcome two critical challenges in cancer therapy: tumour heterogeneity and systemic toxicity.

## Results and discussion

### Preparation and Characterisation of the QSH

The synthetic route of QSH is depicted in Figure S1. The compound QSH comprises a DHODH inhibitor and a photosensitiser IHcy moiety was linked via a disulfide-containing linker (Figure 1a). Firstly, 2-([1,1′-biphenyl]-4-yl) quinoline-4-carboxylic acid (Q) was converted to Q2S by reaction with 2,2′-disulfanediylbis(ethan-1-ol) (SS) through esterification. Subsequently, Q2S was conjugated with IHcy to yield the final compound QSH (Figure S1). The structure of QSH



 

View Article Online
DOI: 10.1039/D6SC02492K





was fully characterised by $^{1}H$ and $^{13}C$ nuclear magnetic resonance (NMR) spectroscopy and high-resolution mass

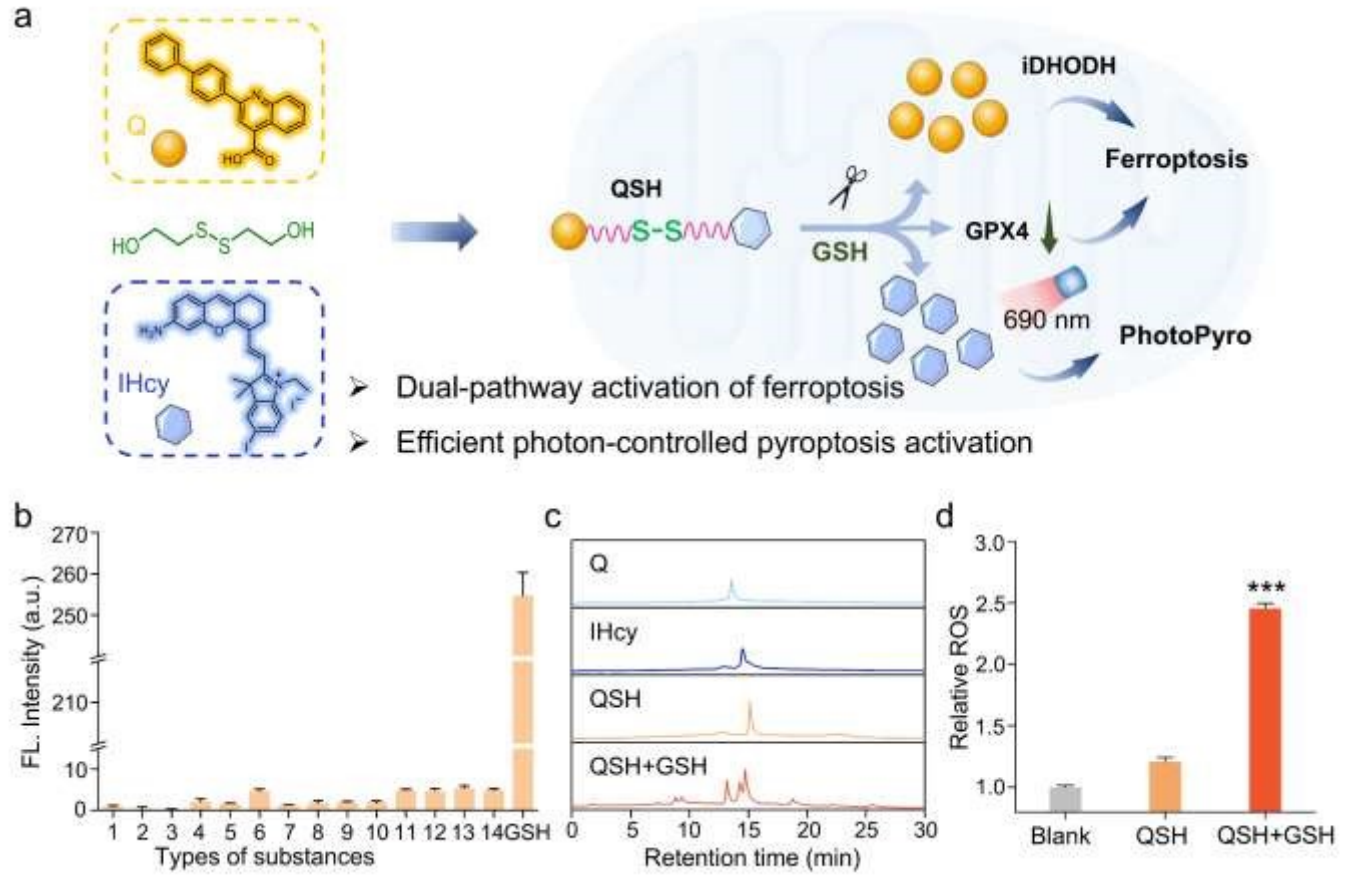


**Figure 1.** Synthesis and characterisation of QSH. a) Diagram of QSH-induced dual cell death modes via three distinct pathways in tumor cells. b) Fluorescence intensity of QSH in the presence of thiols (GSH, 2 mM), non-thiol-containing amino acids (1: histidine, 2: serine, 3: glutamate; 4: HSA, 5: asp, 6: lysine, 7: BSA, 14: tryptophan; 5 mM) and metal ions (8: $Mn^{2+}$, 9: $Fe^{2+}$, 10: $Fe^{3+}$, 11: $Na^{+}$; 12: $Zn^{2+}$,13: $Cu^{2+}$; 1 mM). c) HPLC elution profiles of Q, IHcy, QSH and QSH+GSH. d) Detection of ROS production in different molecular solutions using DCFH. The data are shown as the mean ± s.d. values, ***$P$ < 0.001 by two-tailed Student's t test.

spectrometry (HRMS) (Figures S2-S4).

Next, the spectral properties of QSH were investigated in aqueous solution (10 μM in PBS, pH 7.4). As shown in Figure S5a, the maximum absorption wavelength of QSH exhibited a red shift from 620 to 690 nm following the cleavage of its disulfide bond by GSH. The fluorescence emission of QSH was negligible compared to that of QSH after the GSH reaction (Figure S5b). Notably, this response was observed exclusively in the presence of thiol-containing reagents such as GSH, verifying the specificity of the disulfide bond for GSH (Figure 1b). The cleavage and release process of QSH in the GSH solution was verified by high performance liquid chromatography (HPLC). QSH was co-incubated with GSH at 37 ℃. In the HPLC elution profile of the products (Figure 1c), not only was the QSH peak observed, but it was also accompanied by the appearance of two new peaks, which were determined to correspond to the retention times of Q and IHcy, respectively. To further confirm GSH responsiveness, a fluorescence titration experiment was performed. Upon adding 2 mM GSH to the QSH solution (10 μM), a distinct fluorescence signal emerged at 720 nm, and the solution color changed from blue to green after 180 minutes (Figures S6). The photosensitiser molecules released from QSH under the action of GSH could generate ROS, and this capability was verified using the DCFH probe. As shown in Figure 1d, compared to the blank group, a trace amount of ROS was detected in QSH, while the relative content of ROS in the QSH+GSH solution was approximately 2.5 times that of the blank. Additionally, the ability of QSH to generate ROS was evaluated using 1,3-diphenylisobenzofuran (DPBF) as the probe. Upon irradiation with 690 nm laser (0.05 W $cm^{-2}$) and in the presence of GSH, the absorbance of DPBF at 410 nm decreased rapidly, indicating efficient ROS generation in the QSH+L groups (Figures S7). Furthermore, liquid chromatography-tandem mass spectrometry (LC-MS) analysis of the reaction products revealed clear peaks corresponding to Q-SH (m/z = 386.1214, calcd. 385.11 for $[M+H]^{+}$) and IHcy (m/z = 523.1251, calcd. 523.44 for $[M]^{+}$) at 16 and 8 minutes, respectively (Figure S8), confirming that QSH underwent GSH-induced cleavage to release Q and IHcy.

**Cell Imaging and Cell Viability Evaluation In Vitro**

View Article Online
DOI: 10.1039/D6SC02492K

Given the promising properties of QSH, we next evaluated its cytotoxicity towards cancer cells. Before assessing cytotoxicity, we first verified cellular uptake and the responsiveness of QSH

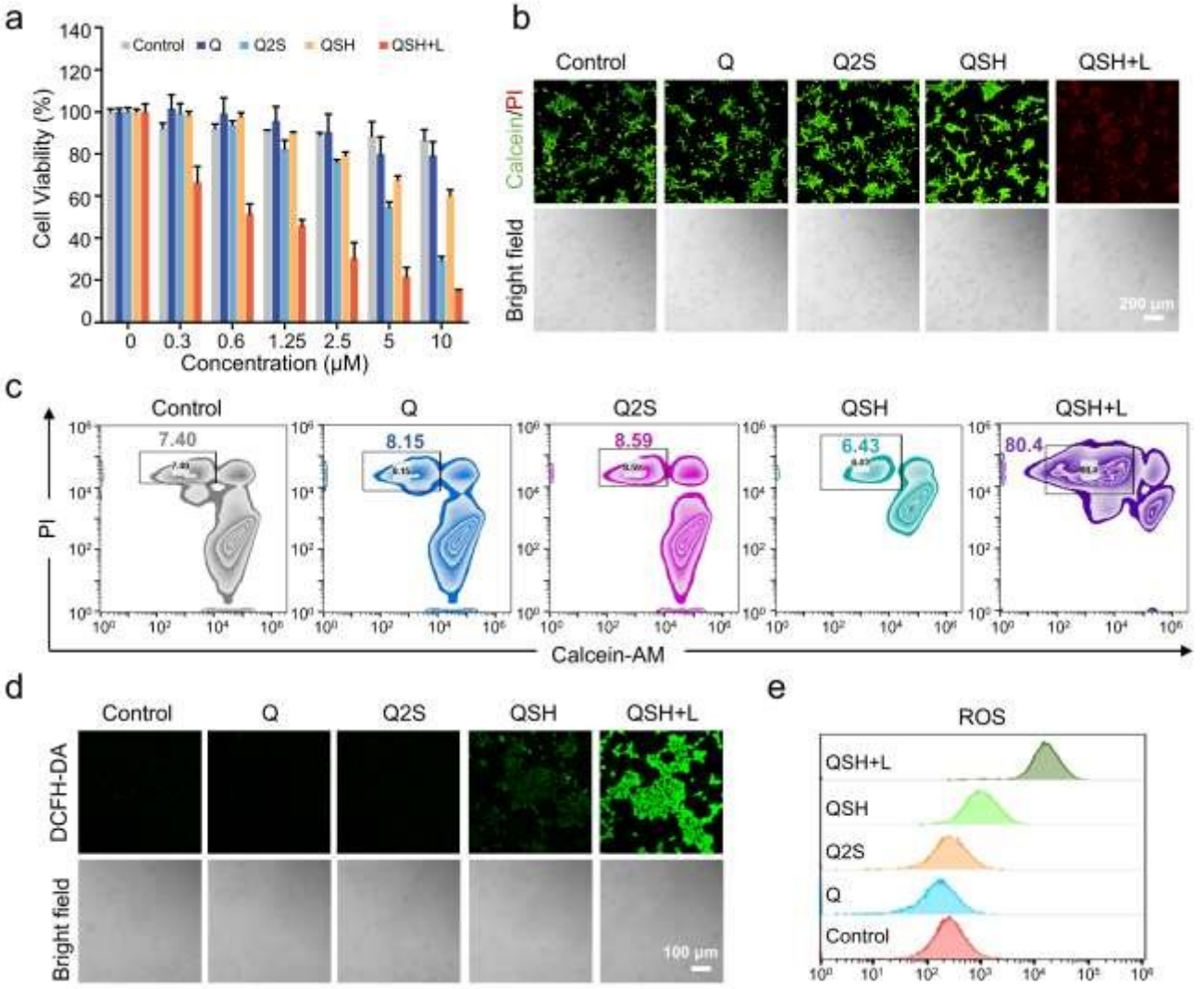


Figure 2. Cytotoxicity of QSH in vitro. a) Cell viability of 4T1 cells incubated with Q, Q2S, and QSH with or without light irradiation (690 nm laser, 0.05 W $cm^{-2}$, 5 min) at various concentrations (n=3 experimental replicates). b) CLSM images demonstrated calcein-AM/PI co-staining of 4T1 cells after incubation with Q, Q2S, and QSH (2.5 μM) with or without light irradiation (690 nm laser, 0.05 W $cm^{-2}$, 5 min) for 24 h. Scale bar: 100 μm. c) Determination of 4T1 cell death via flow cytometry after incubation with Q, Q2S, and QSH (2.5 μM) with or without light irradiation (690 nm laser, 0.05 W $cm^{-2}$, 5 min) for 24 h, respectively. d) CLSM images of DCF-stained tumour cells following treatment with Q, Q2S, and QSH (2.5 μM) with or without light irradiation (690 nm laser, 0.05 W $cm^{-2}$, 5 min) for 4 h. Scale bar: 100 μm. e) Flow cytometry analysis of fluorescence intensity in cells after incubation with Q, Q2S, and QSH (2.5 μM) with or without light irradiation (690 nm laser, 0.05 W $cm^{-2}$, 5 min) for 4 h.

to intracellular GSH using confocal laser scanning microscopy (CLSM). Two cancer cell lines (4T1 and MCF-7) were selected for fluorescence imaging. The fluorescence intensity increased progressively over time and reached its peak at 4 hours. This trend demonstrated that QSH possessed excellent cellular internalisation ability and efficient self-delivery potential (Figures S9 and S10).

Subsequently, the cytotoxicity of QSH was assessed using the standard 3-(4,5- dimethylthiazol-2-yl)-2,5-diphenyltetrazolium bromide (MTT) assay. The half-maximal inhibitory concentration ($IC_{50}$) values of QSH were measured in 4T1, CT26, HepG2 cancer cells, and COS-7 normal cells. Under 690 nm laser irradiation at a power density of 0.05 W $cm^{-2}$ for 5 minutes, the $IC_{50}$ values of QSH towards 4T1, CT26, and HepG2 cells were determined to be 0.79, 1.65, and 2.02 μM, respectively (Figures 2a and S11). Furthermore, A549, HeLa, and MCF-7 cells were utilised to assess the phototoxicity of QSH. The results are presented in Figure S12, showing $IC_{50}$ values of 4.9, 5.75, and 3.09 μM for the respective cell lines. These results confirmed the potent cytotoxicity of QSH + Light (QSH+L) against cancer

View Article Online
DOI: 10.1039/D5SC02492K

cells. Notably, the viability of COS-7 cells remained above 80% even at QSH concentrations up to 10 μM (Figure S13). The results indicated that under specific light irradiation, QSH exerted a significant inhibitory effect on tumour cell proliferation; in contrast, in the absence of light, even at

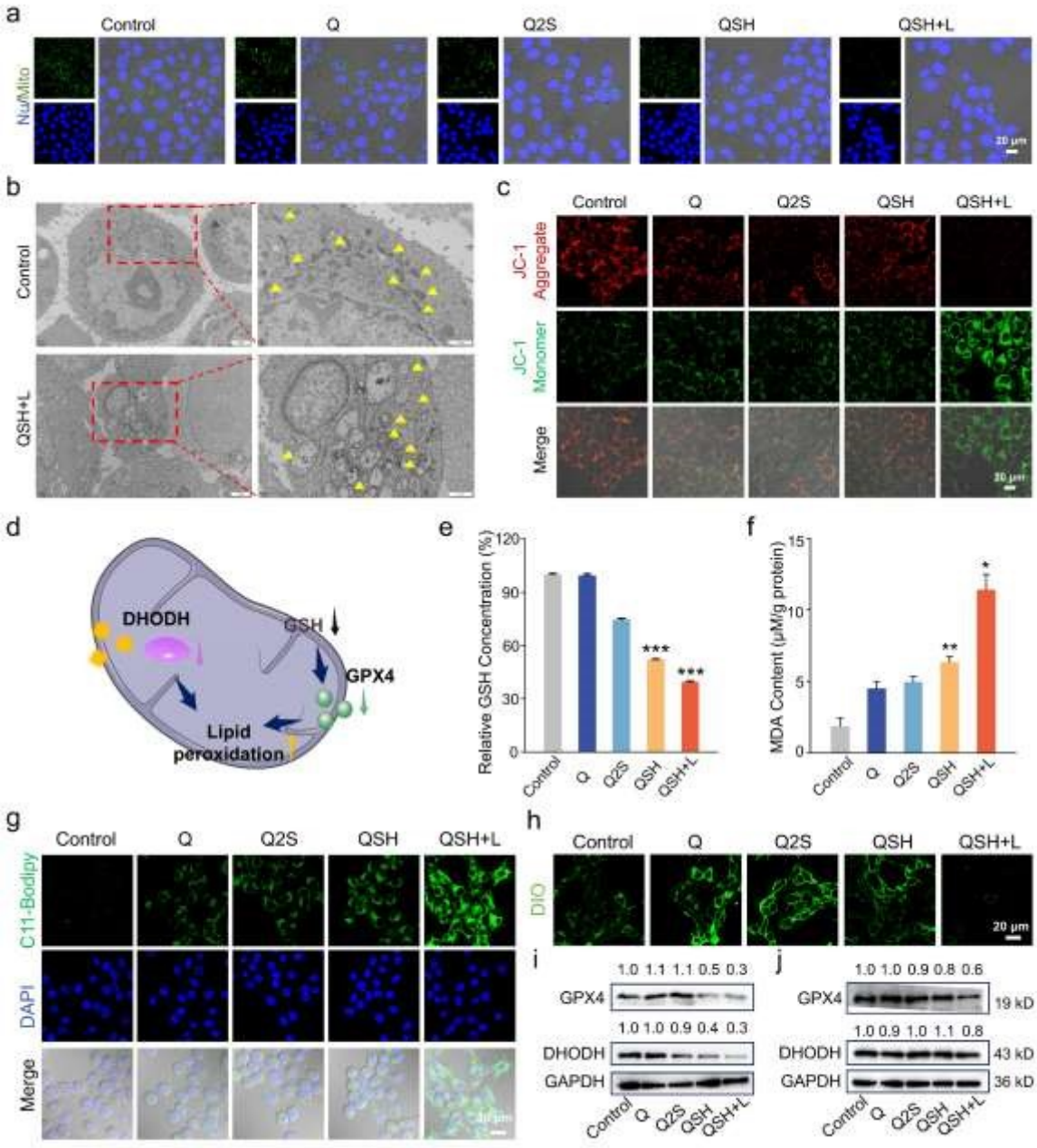


Figure 3. In vitro evaluation of ferroptosis. a) CLSM images of mitochondrial distribution in 4T1 cells following treatment with Q, Q2S, and QSH (2.5 μM) with or without light irradiation (690 nm laser, 0.05 W $cm^{-2}$, 5 min) for 4 h. Scale bar: 20 μm. b) Representative low- and high-magnification TEM images of 4T1 cells incubated with PBS and QSH (2.5 μM), respectively (scale bar: left, 2 μm; right, 1 μm). c) Detection of mitochondrial membrane potential in 4T1 cells with Q, Q2S, and QSH (2.5 μM) with or without light irradiation (690 nm laser, 0.05 W $cm^{-2}$, 5 min) for 4 h. Scale bar: 20 μm. d) Schematic illustration of dual inhibition of antioxidant systems leading to enhanced lipid peroxidation. e) GSH levels in 4T1 cells after treatment with Q, Q2S, QSH (2.5 μM) with or without light irradiation (690 nm laser, 0.05 W $cm^{-2}$, 5 min) for 4 h (n=3 experimental replicates). f) MDA levels in 4T1 cells following treatment with Q, Q2S, and QSH (2.5 μM) with or without light irradiation (690 nm laser, 0.05 W $cm^{-2}$, 5 min) for 4 h (n=3 experimental replicates). g) Cell LPO accumulations in 4T1 cells after co-incubation with Q, Q2S, and QSH (2.5 μM) with or without light irradiation (690 nm laser, 0.05 W $cm^{-2}$, 5 min) for 4 h. Scale bar: 20 μm. h) DIO staining for assessing cell membrane integrity in 4T1 cells after co-incubation with Q, Q2S, QSH (2.5 μM) with or without light irradiation (690 nm laser, 0.05 W $cm^{-2}$, 5 min) for 4 h. i) Western blotting analysis of ferroptosis- related proteins in 4T1 cells after treatment with Q, Q2S, and QSH (2.5 μM) with or without light irradiation (690 nm laser, 0.05 W $cm^{-2}$, 5 min) for 4 h. j) Western blotting analysis of ferroptosis-related proteins in

View Article Online
DOI: 10.1039/D5SC02402K

MCF-7 cells after treatment with Q, Q2S, and QSH (2.5 μM) with or without light irradiation (690 nm laser, 0.05 W $cm^{-2}$, 5 min) for 4 h. The data are presented as mean ± s.d. values, *$P$ < 0.05, **$P$ < 0.01, ***$P$ < 0.001 as determined by two-tailed Student's t-test.

elevated concentrations, its cytotoxicity towards tumour cells was markedly reduced, and minimal adverse effects were observed. This balance between therapeutic efficacy and safety supported the potential of QSH as a safe and effective candidate for cancer treatment.

To explore the basis for the higher sensitivity of 4T1 cells to QSH phototoxicity, we measured GSH levels in various cell lines. As shown in the Figure S14, 4T1 cells exhibit higher intracellular GSH levels compared to several other cancer cell lines. This elevated GSH facilitates more efficient reduction of the disulfide bond, leading to greater release of the active DHODH inhibitor and photosensitizer specifically within 4T1 cells. Given this unique redox environment for drug activation, we selected 4T1 cells for all subsequent mechanistic studies to dissect the pathways of QSH-induced cell death. To furtherassess QSH antiproliferative efficacy, a calcein-AM/propidium iodide (PI) kit was employed for live/dead cell imaging. In this assay, calcein-AM emits green fluorescence in live cells, while PI displays red fluorescence in dead cells. When 4T1 cells were incubated with Q, Q2S, or QSH in the dark, only green fluorescence was detected, indicating minimal cell death. In contrast, strong red fluorescence was observed in cells under both QSH and light conditions, validating the effective cell killing capability of QSH+L (Figure 2b). Additionally, flow cytometry (FCM) analysis provided further validation, showing that apoptotic 4T1 cells percentages were 8.15%, 8.59%, 6.43%, and 80.4% for Q, Q2S, QSH, and QSH+L (2.5 μM), respectively (Figure 2c). These data confirmed that QSH+L induced extensive programmed cell death in 4T1 cells. To confirm ROS generation, intracellular ROS levels were measured using the reactive oxygen indicator 2,7-dichlorodihydrofluorescein diacetate (DCFH-DA). As expected, QSH under 690 nm light irradiation induced significantly stronger green fluorescence than QSH alone, indicating enhanced ROS production (Figures 2d and S15a). By contrast, other treatment groups exhibited negligible fluorescence. Consistent results were obtained by flow cytometry in both 4T1 and MCF-7 cells (Figures 2e and S15b).

**QSH-Induced Ferroptosis in Tumour Cells**

Mitochondria play a pivotal role in the ferroptosis process.[47] To elucidate the mechanism underlying QSH-induced cytotoxicity, we first investigated mitochondrial function. As shown in Figure S16, a strong overlap between the red fluorescence signal of QSH and the green signal of Mito-Tracker Green (a mitochondria-specific probe) was observed in 4T1 cells, with a high Pearson's correlation coefficient (R=0.88). This indicates that QSH predominantly localised to the mitochondria. To assess mitochondrial dysfunction induced by QSH, the distribution of mitochondria was monitored using Mito-Tracker Green. In the QSH+L group, significantly weaker green fluorescence was detected (Figures 3a and S17), implying mitochondrial depletion relative to other treatments. Furthermore, transmission electron microscopy (TEM) observation revealed pronounced morphological changes: in QSH+L-treated cells, mitochondria exhibited atrophy and a reduction in cristae structure (Figure 3b). In addition to damage in mitochondrial morphology and number, the functional integrity of mitochondria was also assessed. Specifically, mitochondrial membrane potential (MMP) was evaluated with the J-aggregate-forming carbocyanine 1 (JC-1) probe. In untreated (Control) cells, JC-1 formed aggregates that emitted strong red fluorescence, reflecting intact mitochondrial potential. In contrast, QSH+L-treated cells exhibited intense green fluorescence, indicating a marked reduction in MMP and severe mitochondrial dysfunction (Figure 3c). Similar trends were observed in MCF-7 cells (Figures S18 and S19). These results demonstrated that QSH+L induced both morphological and functional mitochondrial damage, consistent with the characteristics of ferroptosis.

Given that the GPX4-GSH axis and mitochondrial DHODH-mediated pathway are the key antioxidant defence systems against lipid peroxidation (Figure 3d), we next measured GSH levels and lipid peroxidation levels to verify the activation of the ferroptotic cell death pathway. As shown in Figure 3e, GSH levels were significantly decreased in QSH+L-treated 4T1 cells. Moreover, lipid peroxidation levels, measured by malondialdehyde (MDA) content, was significantly elevated in QSH+L-treated cells (Figure 3f). Parallel trends were observed in MCF-7 cells, where QSH+L treatment also induced GSH depletion and increased MDA levels (Figure S20). To elucidate the cell death mechanism induced by QSH+L, we employed the C11-BODIPY probe to assess intracellular lipid peroxide (LPO) accumulation. As shown in Figure 3g and Figure S21, QSH+L-treated 4T1 cells exhibited significantly stronger green fluorescence than the control group, indicating that targeting mitochondrial ferroptosis defence systems triggered robust lipid peroxidation. Similarly, MCF-7 cells co-incubated with QSH+L also showed significantly increased green fluorescence compared to the other treatment groups (Figure S22).

To further assess the impact on plasma membrane integrity, 3,3'-dioctadecyloxacarbocyanine perchlorate (DIO) staining was employed. Compared to the intact membranes of the control group, QSH+L-treated cells exhibited severely disrupted membrane structures in both 4T1 and MCF-7 cells (Figures 3h and S23, S24). Collectively, these findings suggested that QSH+L efficiently depleted GSH, damaged mitochondrial antioxidant systems, enhanced ROS and LPO accumulation, and ultimately triggered ferroptotic cell death. To explore molecular changes associated with ferroptosis, western blot analysis was performed. The expression levels of GPX4 and DHODH were substantially reduced in both 4T1 and MCF-7 cells following QSH+L treatment, compared with the other treatment groups (Figures 3i, 3j and S25). Specifically, in 4T1 cells, GPX4 and DHODH expression was decreased by approximately sevenfold relative to the Control group. Additionally, compared with QSH alone, their expression was decreased by approximately 40% and 25%, respectively. Additionally, we evaluated the phototoxicity and lipid peroxidation levels of QSH in combination with a ferroptosis inhibitor (Fer-1) and uridine (a pyrimidine nucleoside that bypasses DHODH blockade via the salvage pathway) to directly determine whether DHODH inhibition contributes to

View Article Online
DOI: 10.1039/D6SC02492K

QSH-induced ferroptosis. As shown in Figure S26, uridine supplementation significantly rescued QSH-induced cell death (viability increased from 27% to 66%). Similarly, co-treatment

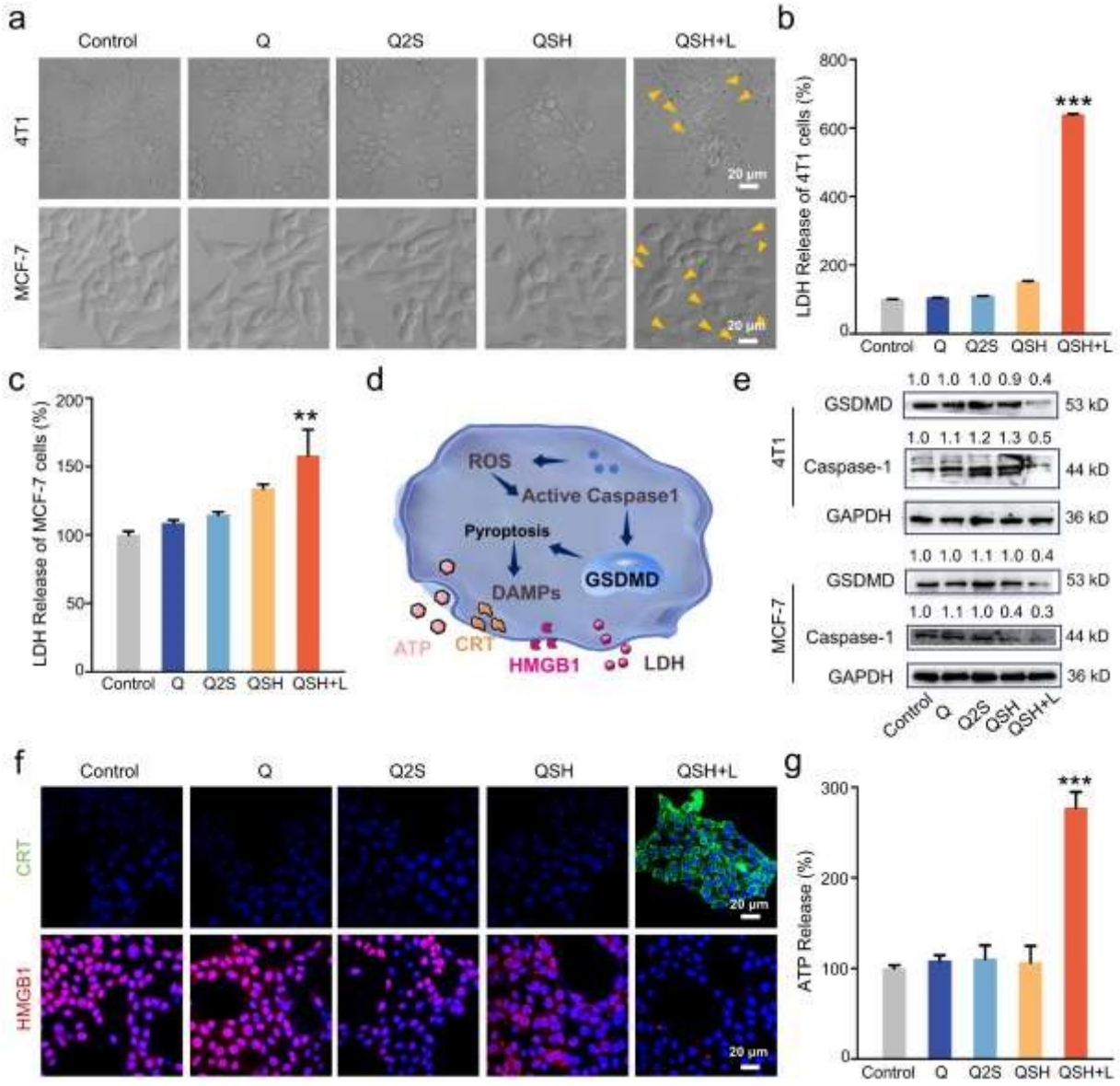


Figure 4. In vitro pyroptosis evaluation. a) Bright-field confocal images of 4T1 cells and MCF-7 cells after exposure to light or no light (690 nm laser, 0.05 W $cm^{-2}$, 5 min) and incubation with QSH (2.5 μM). Yellow arrows indicate bubbling from the cell membrane. Scale bar: 20 μm. b) LDH level in 4T1 cells after treatment with Q, Q2S, and QSH (2.5 μM) with or without light irradiation (690 nm laser, 0.05 W $cm^{-2}$, 5 min) for 4 h (n=3 experimental replicates). c) LDH levels in MCF-7 cells after treatment with Q, Q2S, and QSH (2.5 μM) with or without light irradiation (690 nm laser, 0.05 W $cm^{-2}$, 5 min) for 4 h (n=3 experimental replicates). d) Schematic representation of ROS participation in the pyroptosis pathway. e) Western blot analysis of pyroptosis-related proteins in 4T1 cells and MCF-7 cells after treatment with Q, Q2S, and QSH (2.5 μM) with or without light irradiation (690 nm laser, 0.05 W $cm^{-2}$, 5 min) for 4 h. f) CLSM images of CRT and HMGB1 level in 4T1 cells after treatment with Q, Q2S, and QSH (2.5 μM) with or without light irradiation (690 nm laser, 0.05 W $cm^{-2}$, 5 min) for 4 h (blue represents the nucleus). g) ATP release in 4T1 cells after treatment with Q, Q2S, and QSH (2.5 μM) with or without light irradiation (690 nm laser, 0.05 W $cm^{-2}$, 5 min) for 4 h (n=3 experimental replicates). The data are shown as the mean ± s.d. values, $^{**}P < 0.01$, $^{***}P < 0.001$ by two-tailed Student's t test.

with Fer-1 reduced the phototoxicity of QSH by about 49%. Moreover, pretreatment with Fer-1 for 2 h led to a 10% decrease in MDA levels in 4T1 cells upon QSH+L treatment. These results clearly demonstrated that QSH+L inhibited two critical ferroptosis defence mechanisms, GPX4 and DHODH, thereby promoting ferroptotic cell death.

View Article Online
DOI: 10.1039/D5SC02493K

**QSH-Induced Pyroptosis in Tumour Cells**

The induction of ferroptosis partially impairs intracellular antioxidant defence, thereby enhancing the efficacy of PDT. Previous studies have shown that ROS produced by PDT can lead to acute inflammation and pyroptosis.[41, 42] This process is termed photon- induced pyroptosis activation (PhotoPyro), a

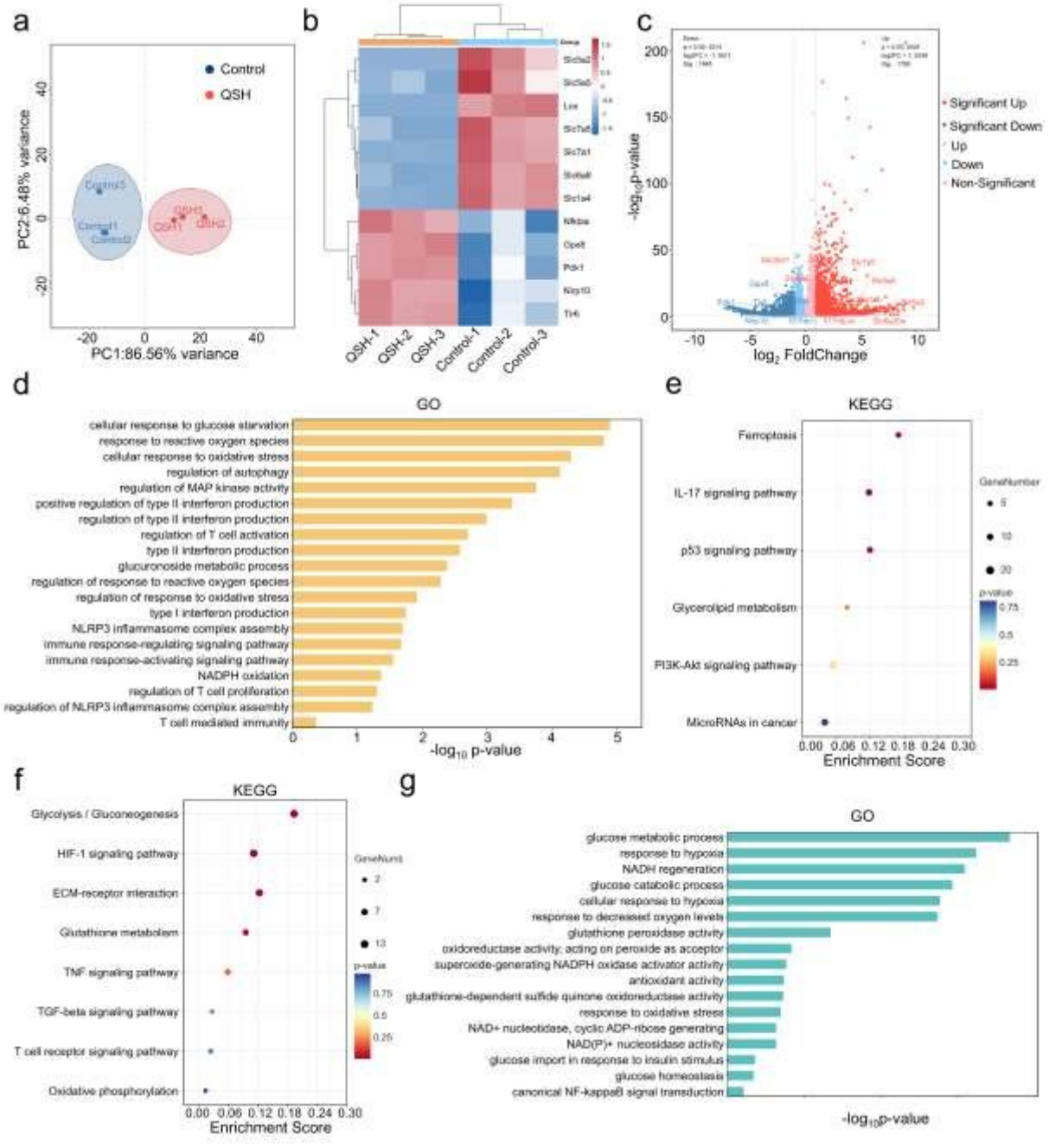


Figure 5. Transcriptional analysis of 4T1 cells after various treatments. a) Principal component analysis between different groups (n = 3). b) Cluster diagram of DEGs between the QSH (2.5 μM) + L (690 nm laser, 0.05 W $cm^{-2}$, 5 min) and control group (n=3). c) Volcano plots of the downregulated genes and upregulated genes in the QSH (2.5 μM) + L (690 nm laser, 0.05 W $cm^{-2}$, 5 min) group compared with the control group. d) GO and e) KEGG analyses of the differentially up-expressed genes in the QSH (2.5 μM) + L (690 nm laser, 0.05 W $cm^{-2}$, 5 min) group and the control group. f) KEGG and g) GO analyses of the differentially down-expressed genes in the QSH (2.5 μM) + L (690 nm laser, 0.05 W $cm^{-2}$, 5 min) group and the control group.

highly inflammatory form of PCD characterised by membrane blebbing. In this context, when QSH-treated 4T1 and MCF-7 cells were irradiated with 690 nm light, visible membrane blebbing was observed as indicated by yellow arrows in Figure 4a. This morphological evidence of pyroptosis was further corroborated by the quantification of lactate dehydrogenase (LD H) release, a hallmark of pyroptosis. As shown in Figures 4b and 4c, LDH levels were significantly elevated in QSH+L-treated 4T1 and MCF-7 cells under light irradiation, whereas no substantial change was observed in the PBS, Q, or Q2S groups.

View Article Online
DOI: 10.1039/D5SC02493K



The gasdermin protein family plays an essential role inpyroptosis. In the classical pathway, caspase-1 cleaves gasdermin (GSDMD) to release its N-terminal fragment, which forms pores in the plasma membrane.[28] This process facilitates the release of DAMPs, thereby triggering ICD (Figures 4d). To

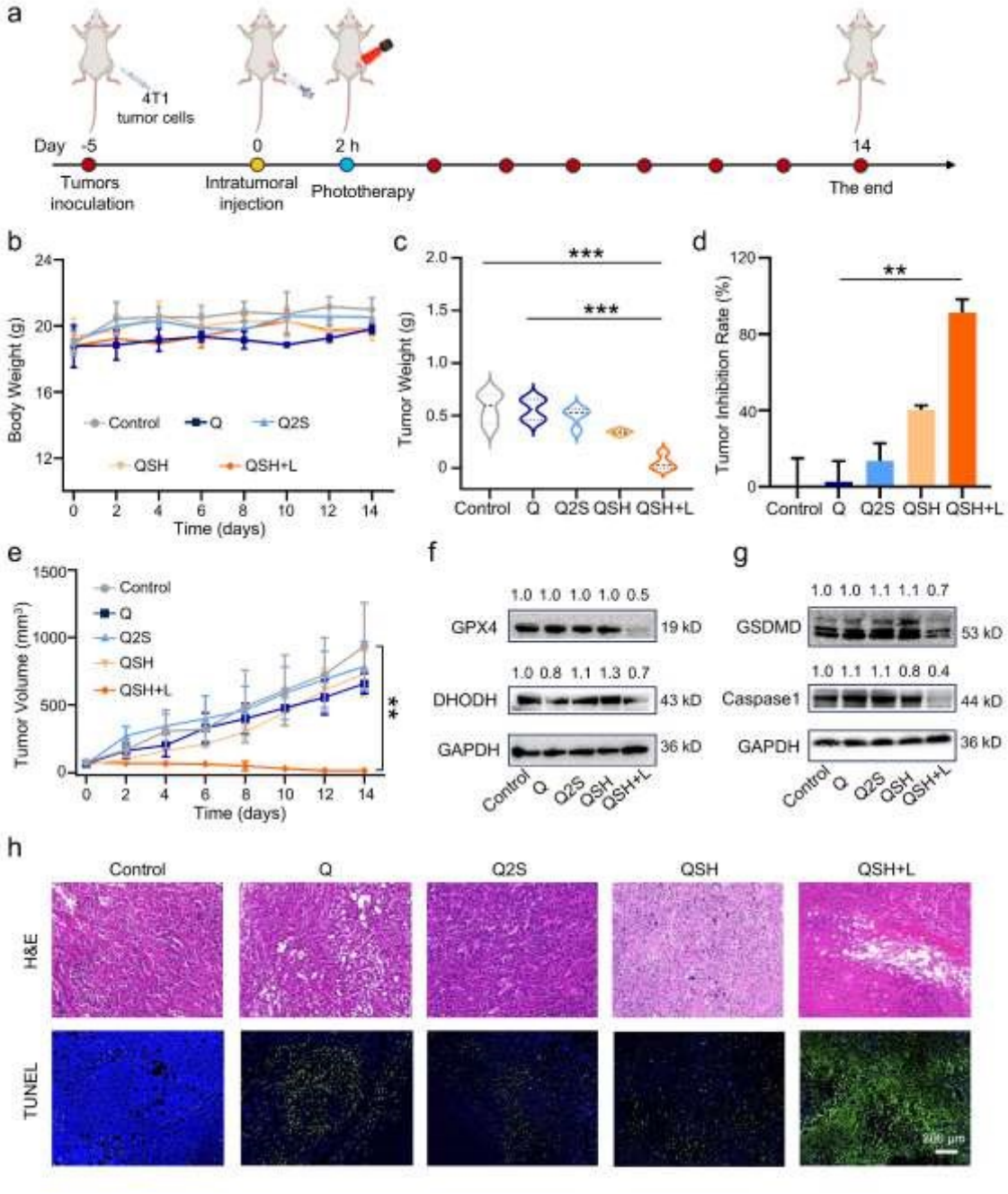


Figure 6. In vivo antitumor ability evaluation. a) Schematic illustration of the treatment schedule of QSH against 4T1 tumours. b) Body weights of the mice in the five treatment groups over 14 days (n=4 experimental replicates). c) The tumour weight of the 4T1 tumour model after 14 days in different groups (n=4 experimental replicates). d) The tumour inhibition rate of the 4T1 tumour weight after 14 days in different groups (n=4 experimental replicates). e) The tumour volume of the 4T1 tumour model after different treatments over 14 days (n=4 experimental replicates). f) Western blotting analysis of ferroptosis related protein levels in tumour tissues after different treatments. g) Western blotting analysis of pyroptosis related protein levels in tumour tissues after different treatments. h) H&E and TUNEL staining of tumour collected from different groups after 14 days. Scale bar, 200 μm. The data are shown as the mean ± s.d. values, $^{**}P < 0.01$, $^{***}P < 0.001$ by two-tailed Student's t test.

confirm QSH+L-induced pyroptosis at the molecular level, western blotting was conducted to assess the expression of pyroptosis-associated proteins. As shown in Figure 4e and Figure S23, QSH+L-treated 4T1 and MCF-7 cells exhibited

View Article Online
DOI: 10.1039/D6SC02402K





significantly lower expression levels of full-length GSDMD and caspase-1 compared with the control group. Specifically, the reductions ranged from 50-60% in 4T1 cells and 60-70% in MCF-7 cells. These results indicate that QSH+L activated GSDMD-mediated pyroptosis via photodynamic stimulation.

To further elucidate the consequences of QSH+L-induced pyroptosis, we assessed the release of canonical immunogenic cell death (ICD) markers at the cellular level. Specifically, we evaluated the exposure of calreticulin (CRT), the translocation of high mobility group box 1 (HMGB1), and extracellular ATP secretion in both 4T1 and MCF-7 cells. The CRT- positive signal was observed in the QSH+L group, and negligible red fluorescence of the nucleus was noted in the QSH+L group, confirming the leakage of HMGB1 from tumour cells (Figures 4f and S27-S28). Similar results were obtained on MCF-7 cells (Figures S29-30). ATP assay results also confirmed the significantly increased ATP secretion in the QSH+L group (Figures 4g and S31). These results supported the presence of ICD-associated features alongside pyroptotic cell death.

To further investigate the crosstalk among the three pathways, we conducted rescue experiments using a ferroptosis inhibitor (Fer-1) and a pyroptosis inhibitor (Ac-YVAD-cmk) in 4T1 cells. The cells were treated with Fer-1 alone, Ac-YVAD-cmk alone, or their combination prior to exposure to QSH under irradiation. As illustrated in Figure S32a, pretreatment with Fer-1 alone improved cell viability from 20.2% to 59.5%, while Ac-YVAD-cmk alone increased viability to about 30.0%. Notably, the combination of both inhibitors further enhanced viability to 72.0%. In terms of lipid peroxidation, Fer-1 alone reduced MDA levels by 20% compared to the QSH+L group, whereas Ac-YVAD-cmk alone resulted in a 15% decrease in MDA levels. LDH release was decreased by about 49% with Fer-1 alone and by approximately 77% with Ac-YVAD-cmk alone. Remarkably, co-treatment with both Fer-1 and Ac-YVAD-cmk restored intracellular MDA and LDH levels to near those observed in the control group (Figure S32b and c). These results indicate that the simultaneous inhibition of both ferroptosis and pyroptosis offers nearly complete protection against QSH+L-induced cell death, thereby confirming that QSH activates both cell death pathways in 4T1 cells.

In summary, these findings highlight that QSH, when combined with NIR light, this approach could simultaneously activate ferroptosis and pyroptosis. The triple pathway strategy targeting the GPX4, DHODH, and GSDMD pathways notably enhanced antitumor efficacy through synergistic mechanisms.

#### Transcriptome sequencing and analysis of Antitumor mechanism

Transcriptome sequencing analysis of QSH+L-treated tumour cells revealed distinct yet partially overlapping gene expression profiles associated with ferroptosis and pyroptosis pathways.

Principal component analysis revealed that the QSH+L treated groups clustered together and were clearly separated from the control group (Figure 5a). A total of 3,735 differentially expressed genes (DEGs) were identified in QSH+L-treated cells ($|\log2FC| > 1$, adjusted $P$-value < 0.05), with 1,790 upregulated and 1,945 downregulated. As demonstrated in Figure 5b, and c, the gene expression of 4T1 cells treated with QSH under 690 nm laser conditions exhibited significant differences compared with the control group. To further explore the biological significance of these DEGs, gene ontology (GO) and Kyoto Encyclopedia of Genes and Genomes (KEGG) pathway analyses were conducted, revealing functional annotations and pathway enrichments associated with the observed mRNA changes. Gene Ontology (GO) analysis demonstrated that QSH+L primarily influenced "redox and inflammatory process", such as reactive oxygen species, T cell activation, NOD-like receptor thermal protein domain associated protein 3 (NLRP3), nicotinamide adenine dinucleotide phosphate (NADPH) oxidation and T cell mediated immunity (Figure 5d). To further validate the core pathways involved in QSH+L action, we performed an extended GO enrichment analysis of the DEGs (Figure S33). The biological process (BP) enrichment confirmed strong enrichment of terms related to glucose and energy metabolism, including glucose metabolic process, glycolytic process, pyruvate metabolic process, and response to hypoxia. Concurrently, terms associated with oxidative stress and ferroptosis-related responses, such as cellular response to oxidative stress and response to reactive oxygen species, were significantly enriched. At the molecular function (MF) level, activities linked to the glutathione-dependent antioxidant system, including glutathione peroxidase activity and antioxidant activity, were prominently altered. These results further corroborate the involvement of metabolic reprogramming and redox imbalance in QSH+L-induced cell death.

KEGG pathway enrichment analysis revealed that the differentially expressed genes (DEGs) identified after QSH+L treatment were predominantly involved in inflammatory and stress-responsive pathways, such as ferroptosis, interleukin-17 (IL-17), p53, and phosphoinositide 3-kinase-protein kinase B (PI3K-Akt) signalling pathways (Figure 5e). These findings suggested a strong link between QSH+L-induced inflammation and oxidative stress-mediated pyroptosis. Intriguingly, metabolic pathways and the hypoxia inducible factor-1 (HIF-1) signalling pathway were also significantly enriched, indicating potential shifts in tumour energy metabolism and oxygen homeostasis following treatment (Figure 5f, g). This was associated with ferroptosis, an inherently metabolic form of cell death. Taken together, these transcriptome data illuminated the molecular mechanisms driving the concurrent activation of ferroptosis and pyroptosis, with potential implications for enhancing tumour therapy.

#### In Vivo Antitumor Efficacy of QSH

Encouraged by the promising in vitro results, we next assessed the antitumor efficacy of QSH+L in vivo. As shown in Figure 6a, a 4T1 tumour-bearing mouse model was established to evaluate the therapeutic potential of QSH+L. Specifically, $5\times10^5$ 4T1 cells were subcutaneously injected into the right flank of mice. After 5 days, when tumour volumes reached approximately 80 $mm^3$, and tumour-bearing mice were randomly divided into five groups, which were intratumorally injected with Control, Q, Q2S, or QSH. Two hours post-injection, the tumours of the QSH+L groups were irradiated with a 690 nm laser (0.1 W $cm^{-2}$) for 10 min. Tumour volumes were measured

 

every 2 days throughout the 14-day treatment period. As illustrated in Figure 6b, the body weights of all mice remained stable across the treatment groups, demonstrating good systemic tolerance and biocompatibility. By comparing the tumour growth in different groups (Figures 6c-6e and S34), it was clear that QSH+L showed the best efficacy among all groups. Throughout the 14-day treatment period, tumour volume maintained an upward trend to varying degrees in all groups except for the QSH+L group. Notably, compared to the control group, the average tumour growth inhibition rate of the QSH+L group was approximately 91%, and some tumours eventually disappeared.

Western blot analysis was employed to confirm the mechanism behind QSH+L's anti-tumour efficacy. Specifically, compared with the control group, tumour tissues from QSH+L-treated mice exhibited significantly decreased expression of key regulatory proteins: GPX4 and DHODH were downregulated by approximately 50% and 30% (Figure 6f), respectively. In addition, the expression levels of caspase-1 and GSDMD were reduced by about 60% and 30%, respectively (Figures 6g and S35). These findings collectively indicated that QSH+L activated both ferroptosis and pyroptosis by modulating three key pathways and were consistent with the in vitro results. Histological evaluations provided further evidence of therapeutic efficacy. Hematoxylin and eosin (H&E) staining of tumor sections from QSH+L-treated mice revealed significant nuclear fragmentation and cellular damage, whereas tumours in the control group retained intact morphology (Figure 6h). Terminal deoxynucleotidyl transferase dUTP nick-end labelling (TUNEL) staining showed markedly enhanced green fluorescence in the QSH+L group, indicating a high proportion of apoptotic cells (Figure 6h). Importantly, biosafety evaluations using H&E staining of major organs and serum biochemical index analysis revealed no significant differences between the QSH+L-treated and the control-treated mice (Figures S36 and S37), suggesting minimal systemic toxicity and excellent safety for in vivo applications. Together, these results demonstrated that QSH+L significantly suppressed tumour growth with minimal systemic toxicity in the 4T1 breast cancer model.

## Conclusions

In this study, we developed a novel unimolecular phototherapeutic agent, QSH, capable of simultaneously inducing ferroptosis and pyroptosis by modulating three distinct pathways. Upon entering redox-stressed cancer cells, QSH accumulated in the mitochondria and was cleaved by GSH through reduction of the disulfide bond, leading to the release of Q and IHcy. TEM and CLSM analyses revealed marked alterations in mitochondrial morphology, accompanied by functional impairment. Intracellular LPO levels were significantly elevated, while glutathione content was reduced. These findings collectively confirmed the induction of ferroptosis. Furthermore, western blot analysis demonstrated downregulation of GPX4 and DHODH, suggesting that ferroptosis was triggered through the suppression of two distinct signalling pathways mediated by GPX4 (the first pathway) and DHODH (the second pathway). Under light irradiation, the formation of pyroptotic membrane blebs was observed via CLSM, providing evidence for the occurrence of pyroptosis. Western blot analysis further revealed downregulation of GSDMD, indicating that pyroptosis was triggered by the GSDMD-mediated signalling pathway (the third pathway), which enhanced the release of DAMPs.

Importantly, ferroptosis and pyroptosis are not mutually exclusive but engage in complex crosstalk through shared molecular nodes.[49] In our study, ROS served as a key molecular link between the two pathways. Lipid peroxidation during ferroptosis activated pyroptotic signalling, while GSDMD pore formation during pyroptosis enhanced ferroptosis sensitivity, forming a positive feedback loop that amplified QSH efficacy. Consistent with our findings, recent studies have demonstrated that both the single-molecule platform and the conductive nanozyme platform successfully harnessed this synergistic effect. [50,51] Overall, this integrated therapeutic strategy, which simultaneously targets three pathways, represents a ROS-centered platform for the coordinated activation of ferroptosis and pyroptosis, overcoming key limitations of conventional therapies, such as low immunogenicity and apoptosis resistance. This approach provides a promising and precise therapeutic modality for addressing tumour heterogeneity and systemic toxicity, thus advancing the development of next-generation cancer treatments.

## Author contributions

X.L., W.-K. L. and J.-L.F. conceived the project and designed the experiments. X.L. and W.-K. L. conducted the synthesis and other characterisation experiments. X.L., and M.-W.Y. analysed the data and co-wrote the manuscript with input from J.-L.F., J.-L.F., H.Z. and X.-J.P. supervised the project. All authors discussed the results and commented on the manuscript.

## Conflicts of interest

The authors declare no competing interests.

## Data availability

The data that support the findings of this study are available in the Supporting Information of this article.

## Acknowledgements

This work was financially supported by the National Natural Science Foundation of China (22338005, 22494701), Ningbo "Innovation Yongjiang 2035" Key R&D Programme (2024Z218, 2024Z185), Liaoning Binhai Laboratory (LBLB-2023-03), the Fundamental Research Funds for the Central Universities (DUT25YG101), Fundamental and Interdisciplinary Disciplines Breakthrough Plan of the Ministry of Education of China (JYB2025XDXM414), and the National Natural Science Foun-dation of China (U25A20619 , 22574041).

## References


1 K. Newton, A. Strasser, N. Kayagaki, V. M. Dixit, *Cell*, 2024, **187**, 235-256.
2 D. Tang, R. Kang, T. Berghe, P. Vandenabeele, G. Kroemer, *Cell Research*, 2019, **29**, 347-364.
3 F. Peng, M. Liao, R. Qin, S. Zhu, C. Peng, L. Fu, Y. Chen, B. Han, *Signal Transduction and Targeted Therapy*, 2022, **7**, 286.
4 Z. Guo, Y. Liu, D. Chen, Y. M. Sun, D. Li, Y. Meng, Q. Zhou, F. Zeng, G. Deng, X. Chen, *Journal of Translational Internal Medicine*, 2025, **13**, 10-32.
5 J. Diao, Y. Jia, E. Dai, *Molecular Cancer*, 2024, 23, 89.
6 F. Du, H. Zhao, Y. Song, Z. Feng, K. Liu, Z. Wang, R. Guo, L. Qiu, Q. Chen, L. Zhou, *Advanced Functional Materials*, 2024, **34**, 2406150.
7 H. Chen, Z. Han, Q. Luo, *Radiation Oncology*, 2022, 17, 196.
8 B. Carneiro, E. WS, *Nature Reviews Clinical Oncology*, 2020, **17**, 395-417.
9 H. He, J. Huang, S. Wu, *Journal of Hematology & Oncology*, 2021, **14**, 171.
10 R. He, Y. Liu, W. Fu, *Molecular Cancer*, 2024, **23**, 267.
11 S. Dixon, K. Lemberg, M. Lamprecht, *Cell*, 2012, **149**, 1060-1072.
12 S. Huang, J. Chung, C. Li, Wu, Yi Qiao, G. To, K. F. Tang, P. Ming-Kuen, *Cancer Letters*, 2024, **604**, 217272.
13 P. Cetraro, J. Plaza-Diaz, A. MacKenzie, F. Abadía-Molina, *Cancers (Basel)*, 2022, **14**, 1671.
14 R. Mirzayans, *Current Issues in Molecular Biology*, 2024, **46**, 5379-5396.
15 W. Zhang, Z. Liu, J. Zhu, Z. Liu, Y. Zhang, G. Qin, J. Ren, X. Qu, *Journal of the American Chemical Society*, 2023, **145**, 16658-16668.
16 L. Huo, S. Zhu, M. Li, M. Tan, M. Fan, J. Zhao, J. Zeng, M. Liu, K. Liu, C. Tong, Z. Zhao, *Advanced Science*, 2025, **12**, 2407713.
17 S. Ji, T. Pan, K. Wang, W. Zai, R. Jia, N. Wang, S. Jia, D. Ding, Y. Shi, *Angewandte Chemie International Edition*, 2025, **64**, e202415735.
18 P. Zhang, Y. Liu, L. Hu, K. Huang, M. Hong, Y. Wang, X. Fan, R. Ulevitch, J. Han, *Science Advances*, 2021, **7**, 9471.
19 K. Xu, M. Chang, Z. Wang, H. Yang, Y. Jia, W. Xu, B. Zhao, Y. Chen, F. Yao, *Advanced Materials*, 2023, **35**, 2302961.
20 T. Ma, L. Liu, Y. Zeng, K. Ding, H. Zhang, W. Liu, Q. Cao, W. Xia, X. Xiong, C. Wu, Z. Mao, *Chemical Science*, 2024, **15**, 9756-9774.
21 P. Liang, L. Ren, Y. Yan, Z. Li, F. Yang, T. Ren, L. Yuan, X. Zhang, *Angewandte Chemie International Edition*, 2025, **64**, e202419376.
22 D. Huang, J. Yin, Y. Zou, H. Huang, S. Long, W. Sun, J. Du, J. Fan, X. Peng, *Smart Molecules*, 2024, **2**, e20240005.
23 Z. Zhao, X. Tong, J. Sun, J. Lu, G. Zhang, Q. Wang, L. Yang, *Smart Molecules*, 2025, **3**, e20250002.
24 S. Van, V. Mashayekhi, H. Bruijn, S. Oliveira, D. Robinson, *Cancers (Basel)*, 2017, 9, 19.
25 S. Banerjee, S. El-Sheikh, A. Malhotra, *Journal of Clinical Medicine*, 2020, **9**, 483.
26 M. Li, J. Kim, H. Rha, S. Son, M. Levine, Y. Xu, J. Sessler, J. Kim, *Journal of the American Chemical Society*, 2023, **145**, 6007-6023.
27 S. Zeng, J. Wang, H. Kang, H. Li, X. Peng, J. Yoon, *Angewandte Chemie International Edition*, 2025, **64**, e202417899.
28 Y. Peng, R. Mo, M. Yang, H. Xie, F. Ma, Z. Ding, S. Wu, J. Lam, J. Du, J. Zhang, Z. Zhao, B. Tang, *ACS Nano*, 2024, **18**, 26140-26152.
29 Y. Zhong, Z. Qiu, K. Zhang, Z. Lu, Z. Li, Y. Cen, S. Li, H. Cheng, *Advanced Materials*, 2025, **37**, 2415078.
30 D. Teng, K. Swanson, R. Wang, *Nature Communications*, 2025, **16**, 3867.
31 S. Wright, P. Kumari, V. Fraile-Ágreda, C. Wang, S. Shivcharan, S. Kappelhoff, E. Margheritis, A. Matz, S. Vasudevan, I. Rubio, M. Bauer, B. Zhou, S. Vanaja, K. Cosentino, J. Ruan, V. Rathinam, *Cell*, 2025, **188**, 280-291.
32 F. Ding, J. Liu, K. Ai, C. Xu, X. Mao, Z. Liu, H. Xiao, *Advanced Materials*, 2024, **36**, 2306419.
33 B. Wang, G. Zhang, Z. Chen, H. Shen, C. Li, J. Li, M. Yi, J. Sun, R. T. K. Kwok, J. W. Y. Lam, A. Qin, B. Z. Tang, *Advanced Materials*, 2025, **37**, 2415673.
34 J. Cheng, L. Li, D. Jin, Y. Dai, Y. Zhu, J. Zou, M. Liu, W. Yu, J. Yu, Y. Sun, X. Chen, Y. Liu, *Advanced Materials*, 2023, **35**, 2210037.
35 W. Wang, S. Yao, J. Luo, C. Ding, Q. Huang, Y. Yang, Z. Shi, J. Lin, Y. Pan, X. Zeng, D. Guo, H. Chen, *Nature Communications*, 2025, **16**, 596.
36 C. Xia, P. Peng, W. Zhang, X. Xing, X. Jin, J. Du, W. Peng, F. Hao, Z. Zhao, K. Dong, M. Tian, Y. Feng, X. Ba, M. Wei, Y. Wang, *Nature Communications*, 2024, **15**, 8971.
37 Z. Wang, X. Wang, X. Dai, T. Xu, X. Qian, M. Chang, Y. Chen, *Advanced Materials*, 2024, **36**, 2312316.
38 X. Zhao, X. Wang, W. Zhang, T. Xu, X. Qian, M. Chang, Y. Chen, *Angewandte Chemie International Edition*, 2024, **63**, e202400829.
39 N. Liu, Q. Lin, Z. Huang, T. Tian, J. Zhang, J. Wang, W. Wei, Z. Guo, J. Zhao, X. Wang, *ACS Nano*, 2024, **18**, 7945-7958.
40 J. Wang, M. Cao, L. Han, C. Liu, J. Qin, Y. Yu, W. Chen, J. Zhang, M. Jiang, X. Gao, S. Huo, X. Zhu, *Journal of the American Chemical Society*, 2024, **146**, 28783-28794.
41 M. Lange, J. Olzmann, S. Ping, Y. Liu, Y. Zhong, C. Chen, G. Wang, X. Chen, M. Lin, M. Lu, Z. Luo, M. He, H. Sung, G. Niu, J. Lam, B. Shi, B. Tang, *Nature*, 2025, **642**, 311-312.
42 N. Liang, Y. Guo, X. Zhang, Y. Ren, Y. He, Z. Liu, D. Xu, S. Xu, *Advanced Science*, 2024, **11**, 2404753.
43 E. Mishima, T. Nakamura, J. Zheng, *Nature*, 2023, 619, 9-18.
44 Z. Fan, S. Wu, H. Deng, G. L. Li, L. H. Huang, H. X. Liu, *ACS Nano*, 2024, **18**, 12261-12275.
45 H. Chen, B. Ding, J. Tan, Q. Meng, J. Li, W. Zhang, P. Zheng, B. Liu, P. Ma, J. Lin, *Angewandte Chemie International Edition*, 2025, **64**, e202501530.
46 C. Liu, L. Guo, Y. Cheng, J. Gao, H. Pan, J. Zhu, D. Li, L. Jiao, C. Fu, *Advanced Science*, 2025, **12**, e17616.
47 N. Liu, Q. Lin, Z. Huang, C. Liu, J. Qin, Y. Yu, W. Chen, J. Zhang, M. Jiang, X. Gao, S. Huo, X. Zhu, *ACS Nano*, 2024, **18**, 7945-7958.

View Article Online
DOI: 10.1039/D6SC02492K

48 Y. Chen, T. Xiong, X. Zhao, J. Du, W. Sun, J. Fan, X. Peng, *Advanced Healthcare Materials*, 2023, **12**, 2202085.
49 W. Zhao, L. Li, F. Ye, J. Zhao, *Journal of Cellular and Molecular Medicine*, 2026, **30**, e71138.
50 S. Yao, F. Xu, Y. Wang, J. Shang, S. Li, X. Xu, Z. Liu, W. He, Z. Guo, Y. Chen, *Journal of the American Chemical Society*, 2025, **147**, 11132-11144.
51 Y. Wang, Zhao, H., Sun, K. D. Deng, G. Liu, L. Li, T. Liu, L. Bao, W. Xu, C. Chen. *Signal Transduction and Targeted Therapy*, 2026, **11**, 96.



View Article Online
DOI: 10.1039/D6SC02492K

The data that support the findings of this study are available from the corresponding author upon reasonable request.